frontiers in Materials

ORIGINAL RESEARCH
published: 12 August 2021
doi: 10.3389/fmats.2021.712500

Strain Rate Effect on Mechanical Properties of the 3D-Printed Metamaterial Foams With Tunable Negative Poisson's Ratio

Di Gao[1,2], Bin Wang[3], Haoqiang Gao[2], Fuguang Ren[4]*, Chunxia Guo[5], Shuai Ma[6], Tiewa Cao[2], Yu Xia[2] and Yansen Wu[2]*

[1]Department of Orthopedics, The Sixth People's Hospital of Anyang, Anyang, China, [2]Tianjin Key Laboratory of Nonlinear Dynamics and Control, Tianjin University, Tianjin, China, [3]Key Laboratory of Soft Soils and Engineering Environment of Tianjin Province, Tianjin Chengjian University, Tianjin, China, [4]School of Mechanical Engineering, Hebei University of Technology, Tianjin, China, [5]Department of Mechanics, School of Science, Xi'an University of Architecture and Technology, Xi'an, China, [6]School of Mathematics and Physics, Qingdao University of Science and Technology, Qingdao, China

As a kind of metamaterial, the negative Poisson's ratio foams, which expand (shrink) in the transverse direction when stretched (compressed) in the longitudinal direction, have many potential applications in fields such as aerospace and mechanical and biomedical engineering. In this paper, the out-of-plane crushing behaviors of four types of the orthogonal isotropic NPR convex-concave foams (CCF) were extensively studied using an electronic universal testing machine and Instron machine at different strain rates where each test was conducted at a constant compressive velocity under uniaxial compression. Strain rate effect on mechanical properties of these foams is experimentally studied. When the strain rate increases, the compressive force enhancement of the foams is obvious and varies with different specimens. The difference in energy absorption and deformation patterns for these foams between quasi-static and dynamic loading conditions is also analyzed. We find that the deformation patterns for the specimens are not only related to the compressive velocities but also the topologies of the specimens. The research in this paper is expected to be meaningful for the optimization design of the foam structures/materials widely used in the fields of aerospace and mechanical and biomedical engineering.

Keywords: convex-concave foams, mechanical properties, strain rate effect, negative Poisson's ratio, optimization design

OPEN ACCESS

Edited by:
Limin Wang,
Yanshan University, China

Reviewed by:
Kai Zhang,
Northwestern Polytechnical University, China
Jiaxi Zhou,
Hunan University, China

****Correspondence:***
Haoqiang Gao
hqgao@tju.edu.cn
Fuguang Ren
renfuguang99@163.com

Specialty section:
This article was submitted to Mechanics of Materials, a section of the journal Frontiers in Materials

Received: *20 May 2021*
Accepted: *21 June 2021*
Published: *12 August 2021*

Citation:
Gao D, Wang B, Gao H, Ren F, Guo C, Ma S, Cao T, Xia Y and Wu Y (2021) Strain Rate Effect on Mechanical Properties of the 3D-Printed Metamaterial Foams With Tunable Negative Poisson's Ratio. Front. Mater. 8:712500. doi: 10.3389/fmats.2021.712500

INTRODUCTION

Negative Poisson's ratio (NPR) foams, which expand (shrink) in the transverse direction when stretched (compressed) in the longitudinal direction, are a typical kind of mechanical metamaterial (Yang et al., 2004). Compared with the conventional foams with positive Poisson's ratio, NPR foams have some enhanced mechanical properties, such as a higher fracture toughness, increased indentation resistance, superior damping and acoustic properties and enhanced sound absorption, and superior tensile fatigue performance (Lakes and Elms, 1993; Chen and Lakes, 1996; Choi and Lakes, 1996; Scarpa et al., 2003; Bezazi and Scarpa, 2007; Zhang et al., 2020b; Zhang et al., 2020c; Zhao et al., 2021).

Mechanical properties play a very important role in engineering applications of the NPR foams. To explore the mechanical properties of the NPR foams and thus promote their practical applications in the fields of vehicle, aerospace, and mechanical engineering, many kinds of NPR foams have been proposed by researchers in recent years. Lakes (1987) first developed novel re-entrant foams with negative Poisson's ratio. Theocaris et al. (1997) used the numerical homogenization theory for the investigation of composite structures with star-shaped inclusions, which are able to exhibit a negative Poisson's ratio. Evans et al. (1994) proposed a re-entrant three-dimensional, open-celled NPR foam. Based on the commercial soft polyurethane foam material as matrix and shape memory epoxy resin as functional phase, Yao et al. (2018) proposed such NPR foams with different re-entrant structures. Adopting an assembly method, Wang et al. (2018b) fabricated 3D double-arrow-head NPR foam structure and studied their mechanical properties. By using an initiator-integrated 3D printing technology, Zhang et al. (2018) introduced metal/polymer re-entrant foams with tunable NPR. Based on a classical re-entrant structure, Chen et al. (2018) proposed three kinds of novel lattice foams with NPR, which showed enhanced energy absorption capacity, stiffness, and strength. Fan et al. (2018) proposed a novel method based on steam penetration and condensation (SPC) process and fabricated foams with negative Poisson's ratio. Using an interlocking assembly method, Wang et al. (2018a) fabricated the three-dimensional re-entrant auxetic foams made from carbon fiber reinforced polymer. Through pressure infiltration technology, Xue et al. (2019) fabricated the Al-based auxetic foams with polymer fillers and investigated their compressive mechanical properties with experimental and finite element analyses methods, which showed higher elastic modulus, compressive strength, and better energy absorption capacity. Through the experimental and finite element methods, Cui et al. (2018) have systematically studied effects of geometrical morphology on elastic moduli, energy absorption, and damage properties of the convex-concave foams (NPR). The CCF are constructed by replacing cell edges of the conventional open cell foams (COF), whose straight cell edges of square cross sections are arranged in planes at forty-five degrees relative to each other (Dolla, 2014), with sin-shaped cell edges of equal mass but different cross sections.

In the practical engineering applications, strain rate effect plays also a vital role in the reliable design of the NPR foams. With respect to strain rate effect of the structural materials, much research work has been done by the researchers all over the world. Baker et al. (1998) investigated the strain rate effect on energy absorption capacity of metal honeycombs through static and dynamic tests. The group of Tao Yong studied the strain rate effect on mechanical behaviour of metallic honeycombs under out-of-plane dynamic compression through theoretical and experimental analyses (Tao et al., 2015a), numerical simulation, and theoretical analysis (Tao et al., 2015b), respectively. Through an experimental analysis, Nia and Sadeghi (2013) investigated the effects of strain rate on the mechanical behaviour of bare and foam-filled honeycomb structures under compression. Adopting a modified Johnson rate dependent model, Tabiei and Wu (2000) investigated the strain rate effect on the dynamic response of wood material. Vural and Ravichandran (2003) studied the influence of strain rate on dynamic and energy dissipation properties of balsa wood through experimental and theoretical analysis. Widehammar (2004) systematically investigated the mechanical properties of spruce wood under different strain rates, moisture content, and loading direction; the strain rate effect on their stress-strain relationships was obtained. Comley and Fleck (2009) conducted experiments on adipose tissue under shear and compression, the strain rate effect on the mechanical properties of porcine adipose tissue was investigated. Guo et al. (2015) proposed a three-dimensional constitutive model to investigate the influence of strain rate on the mechanical properties of the shape memory polymer (epoxy). By conducting experiments on the luffa sponge material under different strain rates, Shen et al. (2013) studied the influence of strain rate on the mechanical properties of luffa sponge. Using an Instron machine and a split Hopkinson pressure bar apparatus, Miao et al. (2016) investigated nanosilica filled epoxies under different strain rates and the effects of strain rate on the mechanical properties of nanosilica/epoxy was analyzed. Pastorino et al. (2007) studied the NPR open cell foams, which showed that the strain rate has a great influence on the stress-strain curves and magnitudes of the Poisson's ratio. Through finite element analysis, Yang et al. (2015) designed a metal foam model and investigated the strain rate effect on the foam structures. Dou et al. (2016) investigated the influence of strain rate on the aluminum foam sandwich panels based on the finite element models.

Taking into account their special properties originating from the effect of NPR, a variety of NPR foams have also been proposed for applications in the medical fields. By using custom-made digital micro-mirror device stereolithography technology, Soman et al. (2012) proposed and fabricated a multi-layer scaffold which exhibited simultaneous negative and positive Poisson's ratio behavior. Choi et al. (2016) fabricated the organic/inorganic composite scaffolds by mixing hydroxyapatite (HA) to poly (lactide-coglycolide) (PLGA) which possess negative Poisson's ratio (NPR) and investigated the mechanical properties and cyto-compatibility of the composite scaffold. Kim et al. (2017) investigated the influence of dynamic compressive stimulation on MG-63 cell proliferation on an auxetic PLGA scaffold which exhibits negative Poisson's ratio. Using the organic-inorganic photopolymer SZ 2080, Flamourakis et al. (2020) fabricated a re-entrant hexagonal geometry scaffold which possess a negative Poisson's ratio with the multiphoton lithography technique. Zhang et al. (2020) designed the unit cells of titanium alloy to mimic trabecular structure and investigated the difference between the design and fabrication of the trabecular structures, as well as mechanical properties and the progressive collapse behavior and failure mechanism of the scaffold. Park et al. (2005) fabricated the polyurethane foam with a negative Poisson's ratio for the insoles of the shoes of diabetic patients. Park et al. (Park and Kim, 2013) designed a structural polyurethane scaffold which exhibits negative Poisson's ratio for cartilage regeneration and the chondrocyte proliferation effectiveness

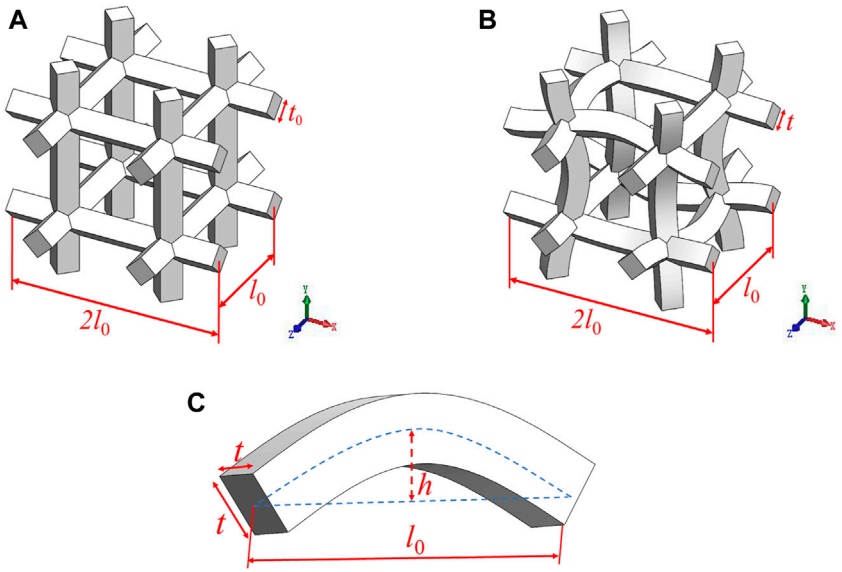

FIGURE 1 | (A) Cubic unit cell model of the conventional open-cell foams, in which the edge thickness is t_0 and the edge length is l_0; **(B)** Cubic unit cell model of the negative Poisson's ratio convex-concave foams; **(C)** Schematic diagram of the sine-shaped cell edges of the convex-concave foams (CCF) with chord span l_0, chord height h, and thickness t.

within the auxetic scaffold under mechanical (compression) stimulation was studied.

Dedicated to promoting their applications in the fields of vehicle, mechanical, aerospace, and medical engineering, in this paper, strain rate effects on mechanical behaviors of the NPR CCF are further systematically studied. In the open literature, mechanical behaviors of the NPR CCF under different compressive loading strain rates are still not clear. In fact, systematic and deep understanding of mechanical behaviors of the NPR CCF under different compressive loading speeds or strain rates is critical for their practical engineering applications. Choosing one conventional foam (COF) and three NPR convex-concave foams (CCF) of equal mass as examples for illustration, strain rate effects on force-displacement curves and energy absorption, the damage patterns of the NPR CCF, and the influence of geometrical morphology on the mechanical properties of NPR foams are experimentally investigated. The study of this paper plays a vital role in the optimization design of the foam structures/materials and facilitates their practical application in engineering fields.

SAMPLES AND EXPERIMENTS

3D-Print of the Negative Poisson's Ratio Convex-Concave Foams

In this paper, one kind of conventional foam and three kinds of NPR convex-concave foams (Cui et al., 2018) are investigated. Cubic unit cell models of the COF and CCF are shown in **Figures 1A,B**, respectively. t_0 and l_0 are the edge thickness and length of the COF, the CCF are constructed by replacing cell edges of the open-cell foam, whose square cross section cell walls are connected in the 45° diagonal direction, and the CCF have sin-shaped cell edges with chord span l_0, chord height h, and side thickness t. By using 3D-printed technology, one type of COF and three kinds of CCF structures with equal quality are printed. As depicted in **Figure 2A**, the four kinds of samples are named COF0, CCF1, CCF2, and CCF3, respectively. They are constructed by 5 × 5 × 7 arrays (**Figure 2B**) of their cubic unit cell (**Figures 1A,B**). The materials of these samples are a type of nylon material (PA2200), whose young's modulus and density (sintered) are 1500 MPa and 930 kg/m^3.

The curve of the sine-shaped cell edges (**Figure 1C**) of the CCF samples can be mathematically described as $y = h\sin(\pi x/l_o)(x \in [0,\ l_0\ ])$. To avoid the intersection of the sine-shaped cell edges, here $h/l_0 < 0.5$is assumed. Define the curve length of the sine-shaped cell edges as s, then s is expressed as:

$$s = \int_0^{l_0} \sqrt{1 + (y')^2}\,dx = \int_0^{l_0} \sqrt{1 + h^2\pi^2/l_0^2\cos^2(\pi x/l_0)}\,dx \qquad (1)$$

According to the equal-mass principle, we have $t^2 s = t_0^2 l_0$, which gives the side thickness t of the sine-shaped cell edges of the CCF samples

$$t = t_0\sqrt{l_0}/\sqrt{\int_0^{l_0} \sqrt{1 + h^2\pi^2/l_0^2\cos^2(\pi x/l_0)}\,dx} \qquad (2)$$

Here, the edge length and edge thickness of the COF0 are t_0 = 1 mm and l_0 = 5 mm. The chord height h of CCF1, CCF2, and CCF3 are 0.5, 1, and 1.5 mm, respectively. Apparently, when h = 0, the CCF becomes the COF. The chord height to span ratio of the COF0, CCF1, CCF2, and CCF3 are 0, 0.1, 0.2, and 0.3, respectively.

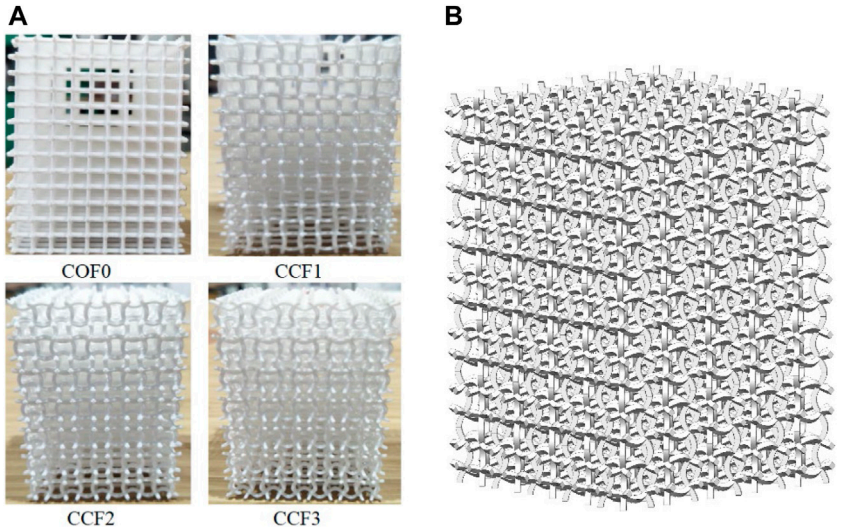

FIGURE 2 | (A) Front views of the COF sample and the corresponding three kinds of CCF samples of equal mass: COF0 (t_0 = 1 mm, l_0 = 5 mm); CCF1 (h = 0.5 mm); CCF2 (h = 1 mm); CCF3 (h = 1.5 mm); **(B)** Schematic diagram of the CCF samples constructed by 5 × 5 × 7 arrays of the cubic unit cell shown in **Panel 1B**.

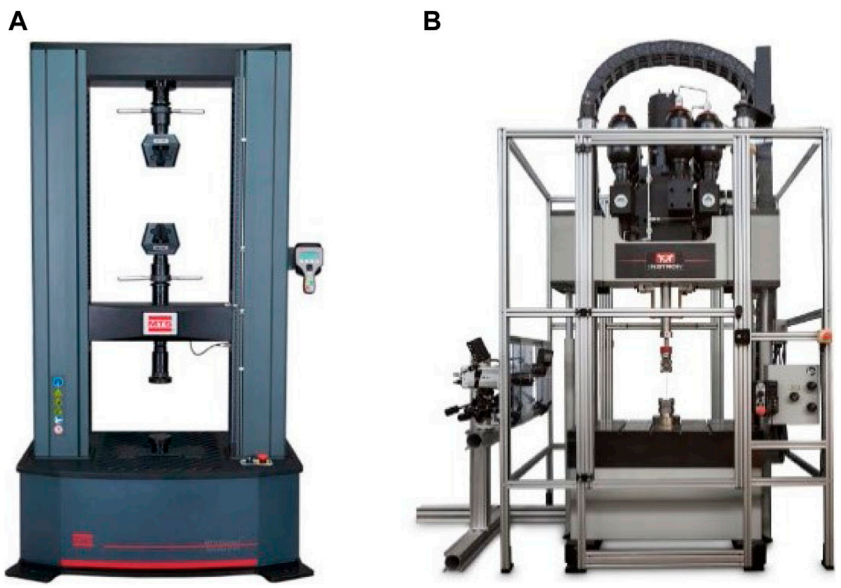

FIGURE 3 | Compressive testing machines for the experiments: **(A)** Universal testing machine for quasi-static tests, **(B)** Instron high rate testing system for dynamic tests.

Quasi-Static Experiments

The quasi-static compression tests were performed in an electronic universal testing machine which has a load capacity of 50 kN, as shown in **Figure 3A**. An iron cylinder with polished upper surface was put on the lower platen and then the foam specimen was placed on the polished surface in order to minimize friction. During the experiment, the lower surface of these specimens was enforced and given normal displacement to move upward to compress the specimen at a constant loading speed of 2 mm/min (3.33×10^{-5} m/s). In the experiment, a computer and digital camera were used to record the displacement and load signals from the testing machine during the entire loading process.

Dynamic Compression Experiments

The dynamic tests were performed using an Instron VHS High Rate Testing System, as shown in **Figure 3B**. The system is equipped with VHS software, which helps to maintain a constant velocity during the compression of the specimens. The Instron machine can achieve a maximum velocity of 20 m/s in

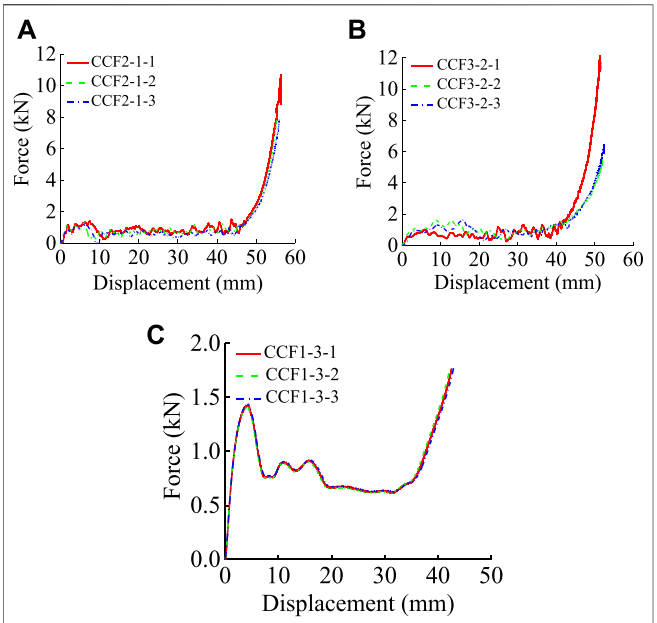

FIGURE 4 | Results of repeated experiments on NPR foams: **(A)** CCF2 ($\dot{\varepsilon}$ =71.4s^{-1}), **(B)** CCF3 ($\dot{\varepsilon}$ =2.14 × 10^{2} s^{-1}) and **(C)** CCF1 ($\dot{\varepsilon}$ =4.76 × 10^{-4} s^{-1}).

compression and has a load capacity of 100 kN. The specimens were placed on the bottom compression platen which was positioned at a considerably long distance from the top platen at the beginning of each test. During the compression, the upper platen moved downwards to impact with the lower fixed platen. Very thin and weak glue was used to stick the specimen to the lower platen in order to avoid any possible slippage of the specimens during the compression. The Instron machine was used on tests under 5 and 15 m/s, for which the corresponding nominal strain rates are 71.4 and 2.14×10^{2} s^{-1}, respectively, for specimens 70 mm high.

In this paper, each experiment was repeated three times at the same condition under quasi-static and dynamic loading for all specimens. **Figure 4** shows the force-displacement curves of three types of NPR foams for three repeated tests under strain rates 71.4, 2.14 × 10^{2} and 4.76 × 10^{-4} s^{-1}. Although the data of compressive force has a slight gap, the overall trend is basically the same and there is good repeatability.

RESULTS AND DISCUSSION

Force-Displacement Curves

In the experiments, four groups of foam specimens, namely COF0, CCF1, CCF2, CCF3, with different h/l_0 ratios were tested at 5 m/s, 15 m/s, and 2 mm/min, for which the corresponding strain rates are 71.4, 2.14 × 10^{2}, and 4.76 × 10^{-2}s^{-1}. Three experiments were conducted for each type of the specimen. **Table 1** gives the characteristics of different foam specimens with different h/l_0 ratios tested. The force-displacement curves for these foams are shown in **Figure 5**. Similar to some metal foams, the force-displacement curves can be divided into three stages, namely, the initial elastic, plastic collapse region, and densification regime. The force of these curves linearly increases with strain up to the elastic limit, then the curve reaches a peak point and becomes non-linear after the elastic limit, after which the force fluctuates during the plastic collapse plateau regime. In these curves, strong fluctuations can be seen in all the dynamic loading tests, but the fluctuation degree of these different specimens is different from each other at the same strain rate. The specimen, COF0, has the most volatile curve and it fluctuates around the *X*-axis. For the other three groups of specimens, CCF1, CCF2, CCF3, their curves are almost all over the *X*-axis and with the increase of the h/l_0 ratio, the degree of the fluctuation in the plateau region decreases. The specimens do not have an evident plateau region compared with metal foams and they have a wavy plateau stress which fluctuates significantly. For the specimen COF0 and CCF1 under dynamic loading, there is a negative value of the force in the curves after the initial peak, which indicates that, after the crushing of the first row of the specimen, there is a spring-back effect of the impactor mass; the reason for this phenomenon may be because of the property of the nylon or the failure modes of these specimens.

TABLE 1 | Summary of the tests on the foams and the results.

Test no	Mass	h/l_0	Velocity (m/s)	Strain rate (s^{-1})	Initial peak force (kN)
COF0-1-1	m	0	5	71.4	3.490
COF0-1-2	m	0	5	71.4	3.837
COF0-1-3	m	0	5	71.4	4.054
COF0-2-1	m	0	15	2.14 × 10^{2}	6.504
COF0-2-2	m	0	15	2.14 × 10^{2}	5.083
COF0-2-3	m	0	15	2.14 × 10^{2}	5.942
COF0-3-1	m	0	3 × 10^{-5}	4.76 × 10^{-4}	1.614
COF0-3-2	m	0	3 × 10^{-5}	4.76 × 10^{-4}	1.756
COF0-3-3	m	0	3 × 10^{-5}	4.76 × 10^{-4}	1.601
CCF1-1-1	m	0.1	5	71.4	3.024
CCF1-1-2	m	0.1	5	71.4	3.307
CCF1-1-3	m	0.1	5	71.4	2.883
CCF1-2-1	m	0.1	15	2.14×10^{2}	3.913
CCF1-2-2	m	0.1	15	2.14 × 10^{2}	4.014
CCF1-2-3	m	0.1	15	2.14 × 10^{2}	3.547
CCF1-3-1	m	0.1	3 × 10^{-5}	4.76 × 10^{-4}	1.425
CCF1-3-2	m	0.1	3 × 10^{-5}	4.76 × 10^{-4}	1.572
CCF1-3-3	m	0.1	3 × 10^{-5}	4.76 × 10^{-4}	1.453
CCF2-1-1	m	0.2	5	71.4	1.377
CCF2-1-2	m	0.2	5	71.4	1.401
CCF2-1-3	m	0.2	5	71.4	1.268
CCF2-2-1	m	0.2	15	2.14×10^{2}	1.724
CCF2-2-2	m	0.2	15	2.14 × 10^{2}	1.875
CCF2-2-3	m	0.2	15	2.14 × 10^{2}	1.691
CCF2-3-1	m	0.2	3 × 10^{-5}	4.76 × 10^{-4}	0.806
CCF2-3-2	m	0.2	3 × 10^{-5}	4.76 × 10^{-4}	0.74
CCF2-3-3	m	0.2	3 × 10^{-5}	4.76 × 10^{-4}	0.794
CCF3-1-1	m	0.3	5	71.4	1.200
CCF3-1-2	m	0.3	5	71.4	1.07
CCF3-1-3	m	0.3	5	71.4	1.214
CCF3-2-1	m	0.3	15	2.14×10^{2}	1.311
CCF3-2-2	m	0.3	15	2.14 × 10^{2}	1.637
CCF3-2-3	m	0.3	15	2.14 × 10^{2}	1.219
CCF3-3-1	m	0.3	3 × 10^{-5}	4.76 × 10^{-4}	0.724
CCF3-3-2	m	0.3	3 × 10^{-5}	4.76 × 10^{-4}	0.751
CCF3-3-3	m	0.3	3 × 10^{-5}	4.76 × 10^{-4}	0.736

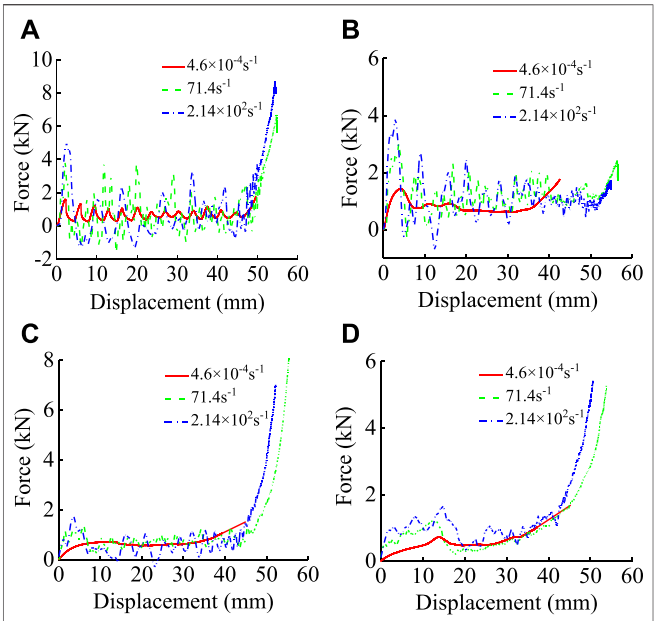

FIGURE 5 | Force-displacement curves for foam specimens under different strain rates: **(A)** COF0, **(B)** CCF1, **(C)** CCF2, **(D)** CCF3.

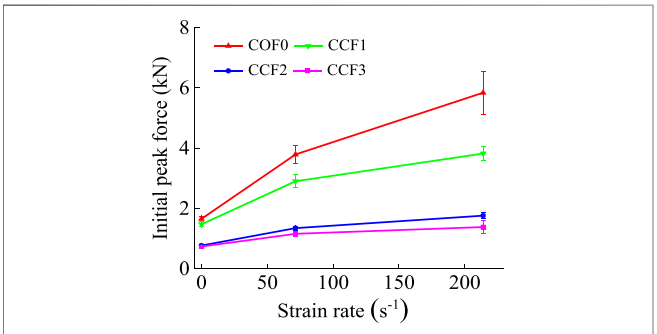

FIGURE 6 | The initial peak force-strain rate curve for the four types of foams: COF0,CCF1, CCF2, and CCF3.

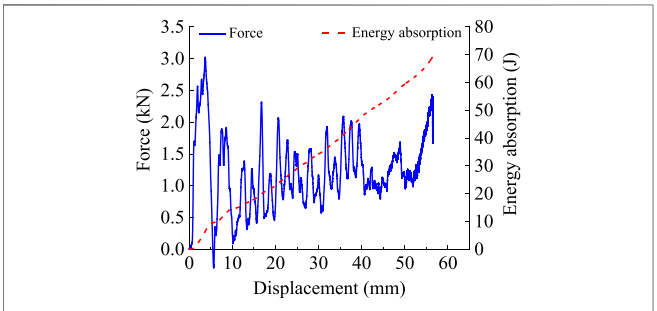

FIGURE 7 | Force and energy absorption-displacement curves for specimen CCF1 at 71.4 s^{-1}.

We can see from the force-displacement curves, compared with the quasi-static compression tests, the increase of the initial peak force under dynamic impact is obvious. The specimen COF0

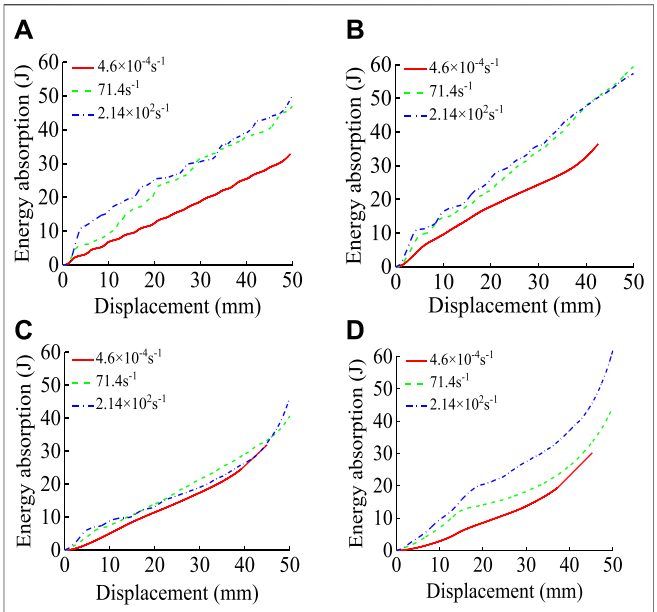

FIGURE 8 | Energy absorption-displacement curves for specimens; **(A)** COF0, **(B)** CCF1, **(C)** CCF2, **(D)** CCF3 under different strain rate.

TABLE 2 | The results of total energy absorption under different strain rates for specimens COF0, CCF1, CCF2, CCF3.

	4.6 × 10^{-4} s^{-1} (J)	71.4 s^{-1} (J)	2.14 × 10^{2} s^{-1} (J)
COF0	26.35	36.64	39.08
CCF1	34.08	48.61	46.98
CCF2	25.47	27.82	26.90
CCF3	22.86	28.50	34.95

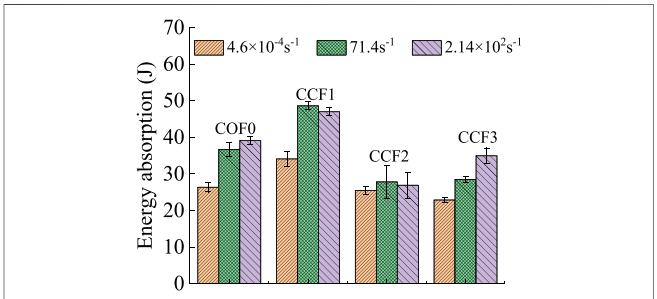

FIGURE 9 | Comparison of energy absorption for the specimens COF0, CCF1, CCF2, and CCF3 under different strain rates.

has the biggest peak force and the plateau region of its force-displacement curve exhibits a marked serration in the plateau region compared with the other three types of specimens, the other three foams have a relatively flat platform stage in their force-displacement curves.

Figure 6 depicts the experimental results of the initial peak force of these foams. We find that the strain rate has a great

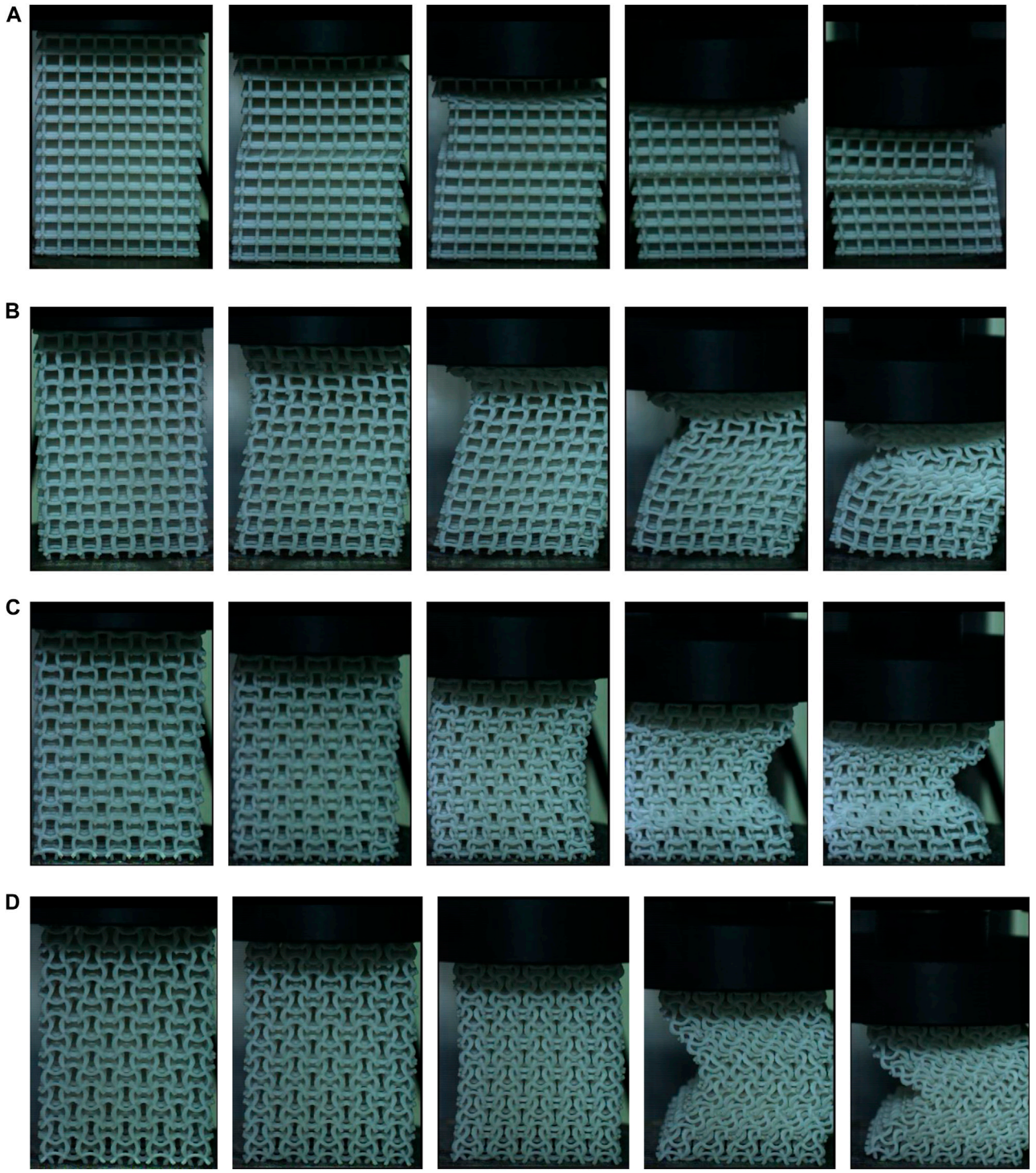

FIGURE 10 | The deformation patterns for the four types of specimens under quasi-static: **(A)** COF0, **(B)** CCF1, **(C)** CCF2, **(D)** CCF3.

influence on the force and such enhancement during the experiments is different between the four types of specimens. It is obvious that the initial peak force of the specimen COF0 under whether quasi-static or dynamic compression is bigger than the ones of these NPR foams. With the strain rate increasing, the peak stress will increase significantly. The peak force enhancement ratio under strain rate 2.14×10^{2} and $71.4^{\circ}s^{-1}$ is 248.8, 157.9, 128.6, 88.0, and 128.9, 107.8, 74.8, 58.4% for the specimen COF0, CCF1, CCF2 and CCF3 compared with the quasi-static compression under strain rate $4.76 \times 10^{-4}\,s^{-1}$,

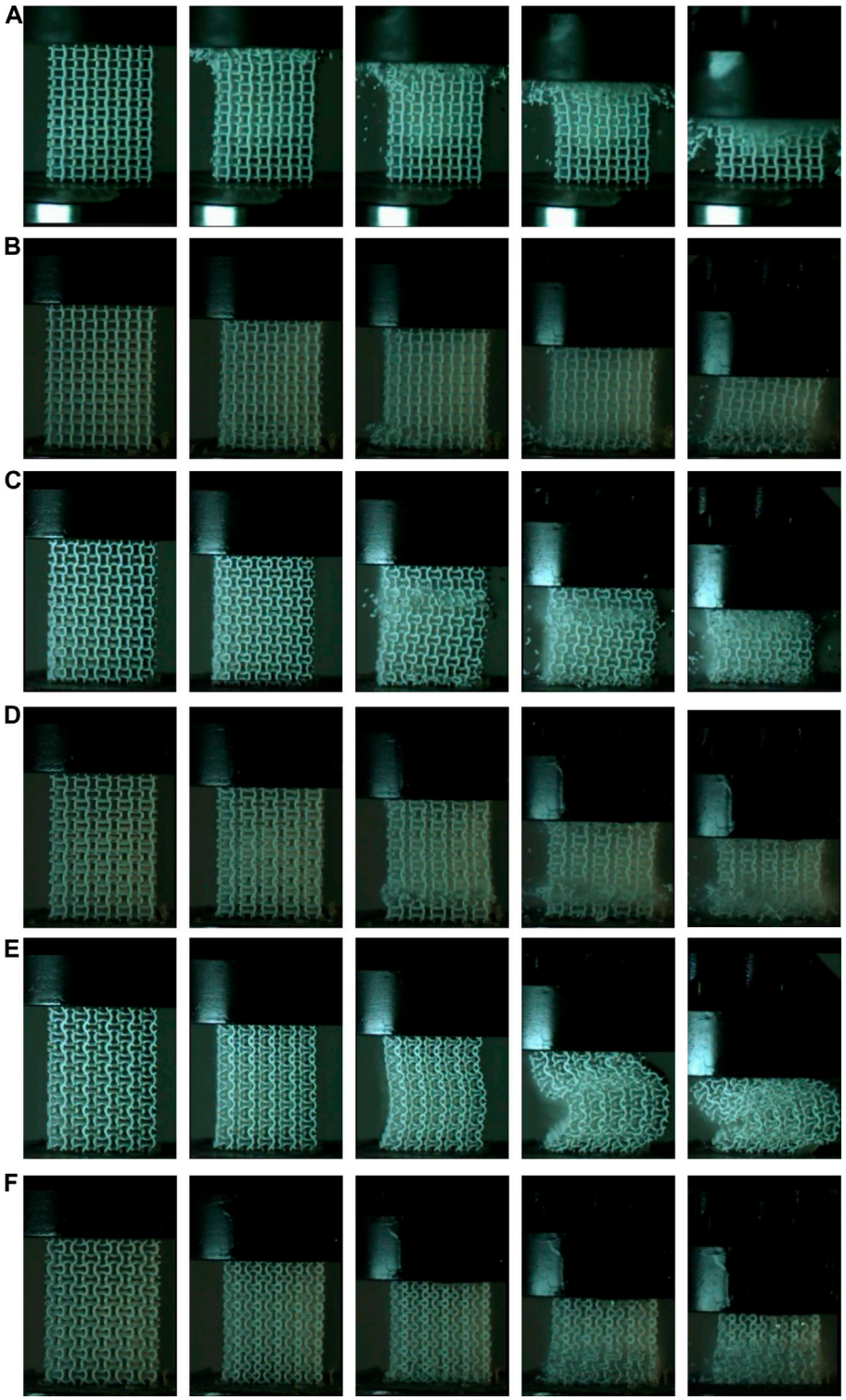

FIGURE 11 | The typical damage patterns for the NPR foams: specimen CCF1 **(A)** $\dot{\varepsilon}$ =71.4 s^{-1} and **(B)** $\dot{\varepsilon}$ =2.14 × 10^2 s^{-1}; specimen CCF2 **(C)** $\dot{\varepsilon}$ = 71.4 s^{-1} and **(D)** $\dot{\varepsilon}$ = 2.14 × 10^2 s^{-1}; specimen CCF3 **(E)** $\dot{\varepsilon}$ = 71.4 s^{-1} and **(F)** $\dot{\varepsilon}$ =2.14 × 10^2 s^{-1}.

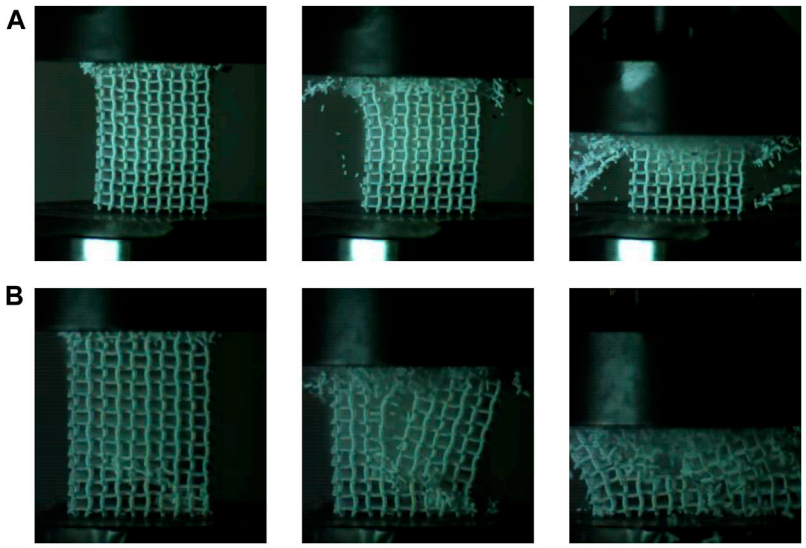

FIGURE 12 | Typical damage pattern for the specimen: **(A)** CCF1-1-1, $\dot{\varepsilon}$ = 71.4 s^{-1} **(B)** CCF1-2-1, $\dot{\varepsilon}$ = 2.14 × 10^2 s^{-1}.

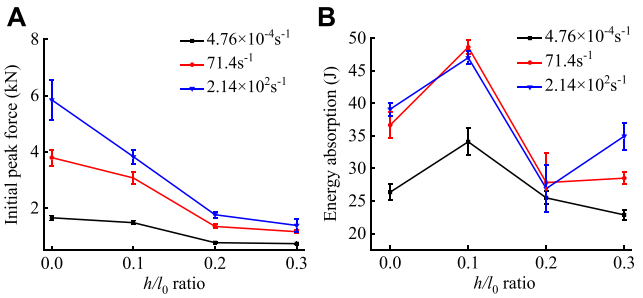

FIGURE 13 | The effects of the topology on the mechanical properties of these foams. **(A)** The quasi-static force-displacement curves for the four types of foams. **(B)** The peak force-h/l_0 ratio curves under different strain rates.

respectively. The force enhancement ratio at strain rate 2.14×10^2 s^{-1} is 54.0, 24.5, 30.8 and 18.7% for the specimen COF0, CCF1, CCF2, and CCF3 compared with the dynamic crushing at strain rate 71.4 s^{-1}, respectively. The conventional specimen COF0 has the largest increase in the force enhancement, which indicates that the conventional foam has a better enhancement capacity compared with the NPR foams. For the three types of NPR foams, the specimen CCF1 has the biggest dynamic enhancement and the specimen CCF3 has the least enhancement ratio compared with quasi-static compression.

Effect of Strain Rate on the Energy Absorption Properties of NPR CCF

Energy absorption (EA) is usually used as an indicator to evaluate the crashworthiness of a structure. By integrating the force-displacement curves of the specimens, the energy absorption is expressed as **Eq. 3**

$$EA = \int_0^d F(x)\,dx \tag{3}$$

where d is the effect total crushing length and F(x) is the crushing force in the force-displacement curves.

Choosing the specimen CCF1 as an example, the plot of compressive force and energy absorption is defined, as shown in **Figure 7**. By calculating the energy absorption of the four types of foams, the energy absorption-displacement curves for specimen COF0, CCF1, CCF2, and CCF3 under different strain rates are plotted in **Figure 8**. Analyzing the plots, the curves under dynamic loading condition for these specimens are above ones in static, which shows a good energy absorption enhancement, it is obvious that the strain rate has a great influence on the capacity of energy absorption of the NPR CCF.

For the specimen COF0, CCF1, and CCF2, the energy absorption curves under 71.4 and 2.14 × 10^2 s^{-1} are very close in the dynamic impact process. For specimen CCF3, when the strain rate increases from 71.4 to 2.14 × 10^2 s^{-1}, the energy absorption enhancement is obvious, which shows that CCF3 has a significant negative Poisson's ratio effect and it is more sensitive to strain rate than the other specimens.

In order to investigate the effect of strain rate on the total energy absorption of these specimens, we defined d = 40 mm as the effective total crushing length and obtained the average total energy absorption values of every specimen which is listed in **Table 2**. As shown in **Figure 9**, the values of energy absorption of these foams under dynamic loading (71.4 and 2.14 × 10^2 s^{-1}) are obviously bigger than the ones under the quasi-static condition (4.6 × 10^{-4} s^{-1}). For the specimen COF0 and CCF1, there is a big enhancement of the energy absorption when strain rate increases from 4.6 × 10^{-4} to 71.4 s^{-1}: 39.05% for COF0 and 42.63% for CCF1. The increase of energy absorption for the CCF2 and CCF3 is 9.23 and 24.67%, which is lower than the specimen COF0 and CCF1. When the strain rate increases from 71.4 to 2.14 × 10^2 s^{-1}, only the

specimen CCF3 has an obvious increase in energy absorption, the values of the specimen COF0 and CCF1 do not change much; the main reason for this could be the specimen CCF3 is relatively sensitive to the strain rate compared to other foams in the experiment.

Damage Patterns Under Quasi-Static and Dynamic Loadings

In the experiments, a high-speed camera was used to record the failure modes of the four types of foams in quasi-static and dynamic loading tests. Damage patterns have a direct relation to the material properties and the geometry topology of the structures. We will display diverse damage patterns under different strain rates later.

For the quasi-static compression, the damage pattern of the specimen COF0 was different from the other three kinds of NPR CCF. During the compression, they first began to buckle from the layer close to the interface near the upper platen and then the middle region of the specimen formed a fold, finally the specimen collapsed layer by layer and its deformation pattern is shown in **Figure 10A**. For the specimens NPR CCF, their deformation patterns were roughly the same. When the experiments began, the specimens CCF1, CCF2, and CCF3 first shrunk continuously and then buckled at the region near the upper platen, finally they displayed global bending. Little rebound was observed in the specimens after unloading and their deformation patterns are shown in **Figures 10B–D**.

For dynamic compression, we found that the damage pattern of the specimen COF0 was similar to one in the quasi-static. When the experiment began, a random layer was destroyed and then collapsed layer by layer until it compacted. For the three types of NPR foams, that may be because of the property of negative Poisson's ratio material, the specimens have a long elastic stage compared with the conventional specimen COF0. When the compression initial peak force is achieved, the specimens are destroyed and their deformation patterns are different from the ones of the specimen COF0. We list the damage patterns of the specimen CCF1, CCF2, and CCF3 under different strain rates respectively, as shown in **Figure 11**.

For the specimen CCF1, when the experiment began, they were first damaged at the layer near the upper or lower platen and then collapsed gradually, as shown in **Figures 11A,B**. Different from the specimen CCF1, the specimen CCF2 was first damaged at a layer near the interfaces between the specimen and platens, then they were crushed layer by layer. The typical deformation patterns of these specimens are shown in **Figures 11C,D**. For the specimen CCF3, they have a bigger h/l_0 ratio than the specimen CCF1 and CCF2; when they were compressed, they first produced a large deformation in the longitudinal direction and became thinner and thinner and then collapsed near the lower platen with the plastic buckling, as shown in **Figure 11F**. There is an interesting phenomenon that the deformation behavior of the specimen CCF3 under strain rate $71.4\ s^{-1}$ as shown in **Figure 11E** is similar to the one in the quasi-static compression as shown in **Figure 10D**.

One interesting deformation pattern should be mentioned, for the specimen CCF1-2-1 and CCF1-1-1, when the experiment began, they first shrunk continuously and then started to break at the layer near the platen and then there was a destruction in the longitudinal direction, finally they collapsed gradually, as shown in **Figure 12**.

Effect of Geometrical Morphology on the Mechanical Properties of the NPR CCF

In this part, the effects of the geometrical parameters on the mechanical properties (the initial peak force and energy absorption) of NPR CCF are studied. As shown in **Figure 13A**, with the fixed strain rates, initial peak force decreases with the h/l_0 increasing from 0 to 0.2. When the strain rate is 4.76×10^{-4} and $71.4\ s^{-1}$, the initial peak force almost keeps a constant value when h/l_0 increases from 0.2 to 0.3. **Figure 13B** depicts the change trend of energy absorption with h/l_0, for fixed strain rates, the energy absorption increases when h/l_0 increases from 0 to 0.1. Under strain rate $4.76 \times 10^{-4}\ s^{-1}$, when the h/l_0 increases from 0.1 to 0.3, the energy absorption decreases. However, for the strain rates 71.4 and $2.14 \times 10^{2}\ s^{-1}$, the energy absorption first decreases with h/l_0 increasing from 0.1 to 0.2 and then increases when h/l_0 increases from 0.2 to 0.3. We can find that CCF1($h/l_0 = 0.1$) has a better capacity of energy absorption compared to other NPR CCF.

CONCLUSION

In this paper, the mechanical properties of the four types of foams have been extensively investigated under different strain rates, namely, 4.76×10^{-4}, 71.4, and $2.14 \times 10^{2}\ s^{-1}$. All tests were conducted at constant compressive velocities and all the specimens are of equal quality and have the same dimension. By analyzing the force-displacement curves, there is an enhancement of initial peak force when the strain rate increases. The influence of strain rate on the energy absorption is also studied. Under quasi-static compression, the conventional foam buckles from the layer close to the upper interface or lower interface and then collapses layer by layer and the other three types of foams first have a lateral contraction and then bend at the section near the middle region. The effect of topologies on the initial peak force and energy absorption is also investigated. The study of this paper provides the theoretical foundations for optimization design of mechanical properties of the NPR CCF and thus could promote their practical applications in the engineering fields.

DATA AVAILABILITY STATEMENT

The original contributions presented in the study are included in the article/supplementary material, further inquiries can be directed to the corresponding authors.

AUTHOR CONTRIBUTIONS

DG, FR, and HG contributed to conception and design of the study. DG, HG, and BW performed the experiment. CG, SM, and TC performed the statistical analysis. DG wrote the first draft of the manuscript. HG, FR, YX, and YW wrote sections of the manuscript.

HG made major contributions to the manuscript revision, proofreading and communication process. All authors contributed to manuscript revision, read, and approved the submitted version.

FUNDING

The research of this paper is supported by Shaanxi Provincial Education Department (Grant No.18JK0437).

REFERENCES

Baker, W. E., Togami, T. C., and Weydert, J. C. (1998). Static and Dynamic Properties of High-Density Metal Honeycombs. *Int. J. Impact Eng.* 21 (3), 149–163. doi:10.1016/S0734-743X(97)00040-7

Bezazi, A., and Scarpa, F. (2007). Mechanical Behaviour of Conventional and Negative Poisson's Ratio Thermoplastic Polyurethane Foams under Compressive Cyclic Loading. *Int. J. Fatigue* 29 (5), 922–930. doi:10.1016/j.ijfatigue.2006.07.015

Chen, C. P., and Lakes, R. S. (1996). Micromechanical Analysis of Dynamic Behavior of Conventional and Negative Poisson's Ratio Foams. *J. Eng. Mater. Technol.* 118 (3), 285–288. doi:10.1115/1.2806807

Chen, Z., Wang, Z., Zhou, S., Shao, J., and Wu, X. (2018). Novel Negative Poisson's Ratio Lattice Structures with Enhanced Stiffness and Energy Absorption Capacity. *Materials* 11 (7), 1095. doi:10.3390/ma11071095

Choi, H. J., Lee, J. J., Lee, J. B., Sung, H.-J., Shin, J.-W., Shin, J. W., et al. (2016). MG-63 Cells Proliferation Following Various Types of Mechanical Stimulation on Cells by Auxetic Hybrid Scaffolds. *Biomater. Res.* 20 (1), 1–8. doi:10.1186/s40824-016-0079-x

Choi, J. B., and Lakes, R. S. (1996). Fracture Toughness of Re-entrant Foam Materials with a Negative Poisson's Ratio: experiment and Analysis. *Int. J. Fract.* 80 (1), 73–83. doi:10.1007/BF00036481

Comley, K., and Fleck, N. (2009). The Mechanical Response of Porcine Adipose Tissue. *ASME J. Biomech. Eng.* 1-30. Available at: http://www-mech.eng.cam.ac.uk/profiles/fleck/papers/259.pdf.

Cui, S., Gong, B., Ding, Q., Sun, Y., Ren, F., Liu, X., et al. (2018). Mechanical Metamaterials Foams with Tunable Negative Poisson's Ratio for Enhanced Energy Absorption and Damage Resistance. *Materials* 11 (10), 1869. doi:10.3390/ma11101869

Dolla, W. (2014). *Rotational Expansion Auxetic Structures*. Kansas: U.S. Patent Application Us3841508, doi:10.1017/cbo9781139946223

Dou, R., Qiu, S., Ju, Y., and Hu, Y. (2016). Simulation of Compression Behavior and Strain-Rate Effect for Aluminum Foam sandwich Panels. *Comput. Mater. Sci.* 112, 205–209. doi:10.1016/j.commatsci.2015.10.032

Evans, K. E., Nkansah, M. A., and Hutchinson, I. J. (1994). Auxetic Foams: Modelling Negative Poisson's Ratios. *Acta Metallurgica et Materialia* 42 (4), 1289–1294. doi:10.1016/0956-7151(94)90145-7

Fan, D., Li, M., Qiu, J., Xing, H., Jiang, Z., and Tang, T. (2018). Novel Method for Preparing Auxetic Foam from Closed-Cell Polymer Foam Based on the Steam Penetration and Condensation Process. *ACS Appl. Mater. Inter.* 10 (26), 22669–22677. doi:10.1021/acsami.8b02332

Flamourakis, G., Spanos, I., Vangelatos, Z., Manganas, P., Papadimitriou, L., Grigoropoulos, C., et al. (2020). Laser-made 3D Auxetic Metamaterial Scaffolds for Tissue Engineering Applications. *Macromol. Mater. Eng.* 305 (7), 2000238. doi:10.1002/mame.202000238

Guo, X., Liu, L., Zhou, B., Liu, Y., and Leng, J. (2015). Influence of Strain Rates on the Mechanical Behaviors of Shape Memory Polymer. *Smart Mater. Struct.* 24 (9), 095009, doi:10.1088/0964-1726/24/9/095009

Kim, M. J., Choi, H. J., Cho, J., Lee, J. B., Sung, H.-J., and Kim, J. K. (2017). MG-63 Cell Proliferation with Static or Dynamic Compressive Stimulation on an Auxetic PLGA Scaffold. *Int. J. Polym. Sci.* 2017, 1–6. doi:10.1155/2017/1286109

Lakes, R. (1987). Foam Structures with a Negative Poisson's Ratio. *Science* 235 (4792), 1038–1040. doi:10.1126/science.235.4792.1038

Lakes, R. S., and Elms, K. (1993). Indentability of Conventional and Negative Poisson's Ratio Foams. *J. Compos. Mater.* 27 (12), 1193–1202. doi:10.1177/002199839302701203

Miao, Y.-G., Liu, H.-Y., Suo, T., Mai, Y.-W., Xie, F.-Q., and Li, Y.-L. (2016). Effects of Strain Rate on Mechanical Properties of Nanosilica/epoxy. *Composites B: Eng.* 96, 119–124. doi:10.1016/j.compositesb.2016.04.008

Nia, A. A., and Sadeghi, M. (2013). An Experimental Investigation on the Effect of Strain Rate on the Behaviour of Bare and Foam-Filled Aluminium Honeycombs. *Mater. Des.* 52, 748–756. doi:10.1016/j.matdes.2013.06.006

Park, K. O., Park, J. C., Choi, J. B., Lee, S. J., Choi, H. H., and Kim, J. K. (2005). Polyurethane Foam with a Negative Poisson's Ratio for Diabetic Shoes. *Kem* 288-289, 677–670. doi:10.4028/www.scientific.net/KEM.288-289.677

Park, Y. J., and Kim, J. K. (2013). The Effect of Negative Poisson's Ratio Polyurethane Scaffolds for Articular Cartilage Tissue Engineering Applications. *Adv. Mater. Sci. Eng.* 2013, 1–5. doi:10.1155/2013/853289

Pastorino, P., Scarpa, F., Patsias, S., Yates, J. R., Haake, S. J., and Ruzzene, M. (2007). Strain Rate Dependence of Stiffness and Poisson's Ratio of Auxetic Open Cell PU Foams. *Phys. Stat. Sol. (B)* 244 (3), 955–965. doi:10.1002/pssb.200572714

Scarpa, F., Ciffo, L. G., and Yates, J. R. (2003). Dynamic Properties of High Structural Integrity Auxetic Open Cell Foam. *Smart Mater. Struct.* 13 (1), 49–56. doi:10.1088/0964-1726/13/1/006

Shen, J., Xie, Y. M., Huang, X., Zhou, S., and Ruan, D. (2013). Behaviour of luffa Sponge Material under Dynamic Loading. *Int. J. Impact Eng.* 57, 17–26. doi:10.1016/j.ijimpeng.2013.01.004

Soman, P., Lee, J. W., Phadke, A., Varghese, S., and Chen, S. (2012). Spatial Tuning of Negative and Positive Poisson's Ratio in a Multi-Layer Scaffold. *Acta Biomater.* 8 (7), 2587–2594. doi:10.1016/j.actbio.2012.03.035

Tabiei, A., and Wu, J. (2000). Three-dimensional Nonlinear Orthotropic Finite Element Material Model for wood. *Compos. Structures* 50 (2), 143–149. doi:10.1016/S0263-8223(00)00089-1

Tao, Y., Chen, M., Chen, H., Pei, Y., and Fang, D. (2015a). Strain Rate Effect on the Out-Of-Plane Dynamic Compressive Behavior of Metallic Honeycombs: Experiment and Theory. *Compos. Structures* 132, 644–651. doi:10.1016/j.compstruct.2015.06.015

Tao, Y., Chen, M., Pei, Y., and Fang, D. (2015b). Strain Rate Effect on Mechanical Behavior of Metallic Honeycombs under Out-Of-Plane Dynamic Compression. *J. Appl. Mech.* 82 (2). doi:10.1115/1.4029471

Theocaris, P. S., Stavroulakis, G. E., and Panagiotopoulos, P. D. (1997). Negative Poisson's Ratios in Composites with star-shaped Inclusions: a Numerical Homogenization Approach. *Archive Appl. Mech. (Ingenieur Archiv)* 67 (4), 274–286. doi:10.1007/s004190050117

Vural, M., and Ravichandran, G. (2003). Dynamic Response and Energy Dissipation Characteristics of Balsa wood: experiment and Analysis. *Int. J. Sol. Structures* 40 (9), 2147–2170. doi:10.1016/S0020-7683(03)00057-X

Wang, X.-T., Chen, Y.-L., and Ma, L. (2018a). The Manufacture and Characterization of Composite Three-Dimensional Re-entrant Auxetic Cellular Structures Made from Carbon Fiber Reinforced Polymer. *J. Compos. Mater.* 52 (23), 3265–3273. doi:10.1177/0021998318764021

Wang, X.-T., Wang, B., Wen, Z.-H., and Ma, L. (2018b). Fabrication and Mechanical Properties of CFRP Composite Three-Dimensional Double-Arrow-Head Auxetic Structures. *Composites Sci. Technology* 164, 92–102. doi:10.1016/j.compscitech.2018.05.014

Widehammar, S. (2004). Stress-strain Relationships for spruce wood: Influence of Strain Rate, Moisture Content and Loading Direction. *Exp. Mech.* 44 (1), 44–48. doi:10.1007/BF02427975

Xue, Y., Wang, W., and Han, F. (2019). Enhanced Compressive Mechanical Properties of Aluminum Based Auxetic Lattice Structures Filled with Polymers. *Composites Part B: Eng.* 171, 183–191. doi:10.1016/j.compositesb.2019.05.002

Yang, B., Liu, Z. J., Tang, L. Q., Jiang, Z. Y., and Liu, Y. P. (2015). Mechanism of the Strain Rate Effect of Metal Foams with Numerical Simulations of 3D Voronoi Foams during the Split Hopkinson Pressure Bar Tests. *Int. J. Comput. Methods* 12 (04), 1540010. doi:10.1142/S0219876215400101

Yang, W., Li, Z.-M., Shi, W., Xie, B.-H., and Yang, M.-B. (2004). Review on Auxetic Materials. *J. Mater. Sci.* 39 (10), 3269–3279. doi:10.1023/b:jmsc.0000026928.93231.e0

Yao, Y., Luo, Y., Xu, Y., Wang, B., Li, J., Deng, H., et al. (2018). Fabrication and Characterization of Auxetic Shape Memory Composite Foams. *Composites Part B: Eng.* 152, 1–7. doi:10.1016/j.compositesb.2018.06.027

Zhang, C., Zhang, L., Liu, L., Lv, L., Gao, L., Liu, N., et al. (2020). Mechanical Behavior of a Titanium alloy Scaffold Mimicking Trabecular Structure. *J. Orthop. Surg. Res.* 15 (1), 1–11. doi:10.1186/s13018-019-1489-y

Zhang, D., Xiao, J., Yu, W., Guo, Q., and Yang, J. (2018). Hierarchical Metal/polymer Metamaterials of Tunable Negative Poisson's Ratio Fabricated by Initiator-Integrated 3D Printing (i3DP). *Nanotechnology* 29 (50), 505704. doi:10.1088/1361-6528/aae283

Zhang, K., Zhao, C., Zhao, P., Luo, J., and Deng, Z. (2020b). Wave Propagation Properties of Rotationally Symmetric Lattices with Curved Beams. *The J. Acoust. Soc. America* 148 (3), 1567–1584. doi:10.1121/10.0001918

Zhang, K., Zhao, P., Zhao, C., Hong, F., and Deng, Z. (2020c). Study on the Mechanism of Band gap and Directional Wave Propagation of the Auxetic Chiral Lattices. *Compos. Structures* 238, 111952. doi:10.1016/j.compstruct.2020.111952

Zhao, P., Zhang, K., Zhao, C., and Deng, Z. (2021). On the Wave Propagation Properties and Poisson's Ratio of the Star-3/6 Structures. *Compos. Structures* 270, 114089. doi:10.1016/j.compstruct.2021.114089

Conflict of Interest: The authors declare that the research was conducted in the absence of any commercial or financial relationships that could be construed as a potential conflict of interest.